catalysts

MDPI

Article

Hollow Co_3O_4 Nanoreactors for Selective Catalytic Oxidation of Emerging Contaminants via Electron-Transfer-Mediated Peroxydisulfate Activation

Yuzhe Wang [1], Yumeng Pang [2], Chunke Zhao [2], Gen Wang [2,*] and Pengkang Jin [1,*]

[1] School of Human Settlements and Civil Engineering, Xi'an Jiaotong University, Xi'an 710049, China; ywang11134@163.com
[2] School of Environmental and Municipal Engineering, Xi'an University of Architecture and Technology, Xi'an 710049, China; pangyumeng1118@163.com (Y.P.); zck152036@163.com (C.Z.)
* Correspondence: wanggen@xauat.edu.cn (G.W.); pkjin@xjtu.edu.cn (P.J.)

Abstract

The selective removal of electron-rich emerging organic contaminants (EOCs) from aquatic environments remains a critical challenge, as conventional radical-based oxidation processes suffer from poor selectivity and interference from background constituents. To address this issue, we report an electron-transfer-mediated catalytic oxidation system using peroxydisulfate (PDS) activated by hollow multi-shelled Co_3O_4 (HoMS Co_3O_4) nanoreactors derived from plant-based tannic acid. The triple-shelled hollow architecture affords a high specific surface area with abundant accessible active sites, enabling the HoMS Co_3O_4/PDS system to achieve complete bisphenol A (BPA, 0.04 mM) removal within 90 min (k = 0.045 min^{-1}). Mechanistic investigations, integrating electron paramagnetic resonance spectroscopy, radical quenching, electrochemical analyses and in situ Raman/FTIR spectroscopy, reveal that the degradation proceeds via an electron-transfer-mediated non-radical pathway, in which surface-complexed PDS serves as the primary reactive species. This pathway enables selective oxidation of electron-rich pollutants and endows the system with broad pH adaptability, strong resistance to coexisting water constituents, and robust performance in real water matrices (>93% BPA removal). Moreover, the system maintains stable operation in a continuous flow-through reactor over 72 h with negligible Co^{2+} leaching, offering a sustainable strategy for the selective remediation of EOC-contaminated waters.

Keywords: heterogeneous catalysis; selective catalytic oxidation; electron transfer regime; non-radical oxidation; emerging organic contaminants; hollow multi-shelled Co_3O_4

Check for updates

Academic Editor: Enric Brillas

Received: 26 July 2026
Revised: 18 August 2026
Accepted: 20 August 2026
Published: 22 August 2026

Copyright: © 2026 by the authors. Licensee MDPI, Basel, Switzerland. This article is an open access article distributed under the terms and conditions of the Creative Commons Attribution (CC BY) license.

1. Introduction

The widespread occurrence of emerging organic contaminants (EOCs) such as endocrine-disrupting chemicals, pharmaceuticals, and personal care products in water bodies has raised grave concerns due to their persistence, bioaccumulation potential, and adverse effects on both aquatic ecosystems and human health [1–3]. Conventional biological treatment processes are often inadequate for the complete removal of these recalcitrant pollutants, necessitating the development of advanced remediation technologies [4–6]. Among various approaches, persulfate-based advanced oxidation processes (PS-AOPs) have garnered considerable attention owing to their strong oxidizing capacity, broad operational pH range, and favorable chemical stability of persulfate [7–9]. However, traditional PS-AOPs

that rely on radical species ($SO_4^{\bullet-}$ and $^{\bullet}OH$) suffer from inherent limitations, including poor selectivity, susceptibility to scavenging by background water constituents (e.g., halide ions and natural organic matter), and the formation of potentially toxic byproducts [10–12]. These challenges underscore the urgent need for alternative oxidation pathways that can achieve selective and efficient EOC removal in complex water matrices.

In recent years, non-radical oxidation pathways, particularly electron-transfer processes (ETP), have emerged as promising alternatives to radical-based systems [13–15]. In ETP-mediated persulfate activation, the catalyst facilitates the formation of a surface-activated persulfate complex that directly abstracts electrons from adsorbed organic pollutants, thereby circumventing the generation of free radicals [16–18]. This mechanism confers several distinct advantages, including high selectivity toward electron-rich contaminants, remarkable resistance to inorganic anions and natural organic matter, and reduced oxidant consumption [16,19]. Consequently, considerable efforts have been devoted to the development of efficient heterogeneous catalysts capable of promoting ETP-based persulfate activation for the selective oxidation of target pollutants.

Transition metal oxides, particularly Co_3O_4, have been extensively studied as effective catalysts for persulfate activation owing to their excellent redox properties, natural abundance and cost-effectiveness [19–21]. Nevertheless, conventional Co_3O_4 nanoparticles tend to aggregate in aqueous media, leading to diminished active site exposure and compromised catalytic performance [11,21]. To address this issue, the construction of hollow nanostructures has been recognized as an effective strategy to enhance catalytic efficiency [22–24]. Hollow multi-shelled structures (HoMS) offer several compelling advantages, including high specific surface areas, well-defined internal void spaces, and permeable shell architectures [25–27]. More importantly, the hollow cavities can spatially confine reactants, increasing their local instantaneous concentrations and promoting collision frequency, a phenomenon known as the nanoconfinement effect that substantially accelerates reaction kinetics [28–30]. Despite these merits, the synthesis of HoMS metal oxides often relies on complex templating procedures that limit their scalability and practical application [31–33]. Recently, a self-templating strategy using metal–organic frameworks (MOFs) as precursors has been proposed to prepare hollow metal oxides by pyrolysis [34–36]. However, the high cost of MOFs such as ZIF-8 and ZIF-67 limits their large-scale production and application [37–39]. Hence, developing low-cost synthetic routes for hollow metal oxides remains highly desirable.

In this work, we synthesized HoMS Co_3O_4 with mesoporous shells and a high specific surface area using nature-abundant tannic acid as the precursor. This self-templating strategy not only greatly simplifies the preparation procedure compared to conventional soft or hard templating methods, but also offers a more sustainable and economically viable route [40–42]. Using bisphenol A (BPA) as a model EOC, we systematically evaluated the PDS activation performance of the HoMS Co_3O_4 nanoreactors and elucidated the underlying degradation mechanism via EPR spectroscopy, radical quenching experiments, electrochemical analyses and in situ vibrational spectroscopy (Raman and ATR-FTIR). In addition, the influence of key operational parameters, resistance to common water matrix constituents, and performance in a continuous flow-through system were systematically investigated to assess practical applicability. This work not only provides a cost-effective method for the synthesis of high-performance HoMS Co_3O_4 nanoreactors but also offers comprehensive mechanistic insights into the electron-transfer-based non-radical PDS activation pathway, thereby advancing the development of selective and robust remediation technologies for EOC-contaminated waters.

2. Results and Discussion

2.1. Synthesis and Characterization of HoMS Co_3O_4 Nanoreactors

Figure 1a presents a schematic illustration of the synthesis procedure for HoMS Co_3O_4. The Co-TA polymer was first synthesized via coordination between Co^{2+} and TA molecules and subsequently calcined in air to yield the HoMS Co_3O_4 structure through an Ostwald ripening process, as we reported before [34–36]. During calcination, the near-surface region of the polymer is preferentially oxidized to form a metal oxide shell, while the volume contraction accompanying the polymer-to-oxide conversion generates residual stress that eventually causes shell spallation. Upon prolonged heating, this contraction-spallation cycle proceeds sequentially inward, ultimately yielding the hollow multi-shelled architecture. The morphology and microstructure of the Co-TA precursor and the resultant HoMS Co_3O_4 were examined by SEM and TEM. As shown in Figure 1b, the Co-TA coordination polymer exhibits a uniform spherical morphology with a smooth surface and an average diameter of approximately 180 nm. After calcination at 400 °C in air, the HoMS Co_3O_4 nanoreactors largely retain the spherical shape (Figure 1c), indicating that the thermal treatment does not collapse the overall architecture [40]. Notably, statistical analysis based on SEM images of more than 100 particles (Figure S2a) revealed a decrease in the average particle size to approximately 154.7 ± 18.8 nm (Figure S2c), which is attributable to crystallization-induced contraction during conversion of the metal-polyphenol precursor to crystalline Co_3O_4. The magnified TEM image (Figure 1d) clearly resolves a well-defined triple-shelled hollow structure with substantial internal cavities and thin porous shells, confirming the successful fabrication of the HoMS architecture. The thicknesses of the outer, middle and inner shells were measured to be 8.9 ± 2.3 nm, 6.6 ± 2.7 nm, and 3.2 ± 1.5 nm, respectively. High-resolution TEM (HR-TEM) images obtained from different particles (Figures 1e and S2d) reveal distinct lattice fringes with an interplanar spacing of ~0.24 nm, corresponding to the (311) plane of cubic Co_3O_4 [41–43], which attests to the high crystallinity of the as-prepared sample.

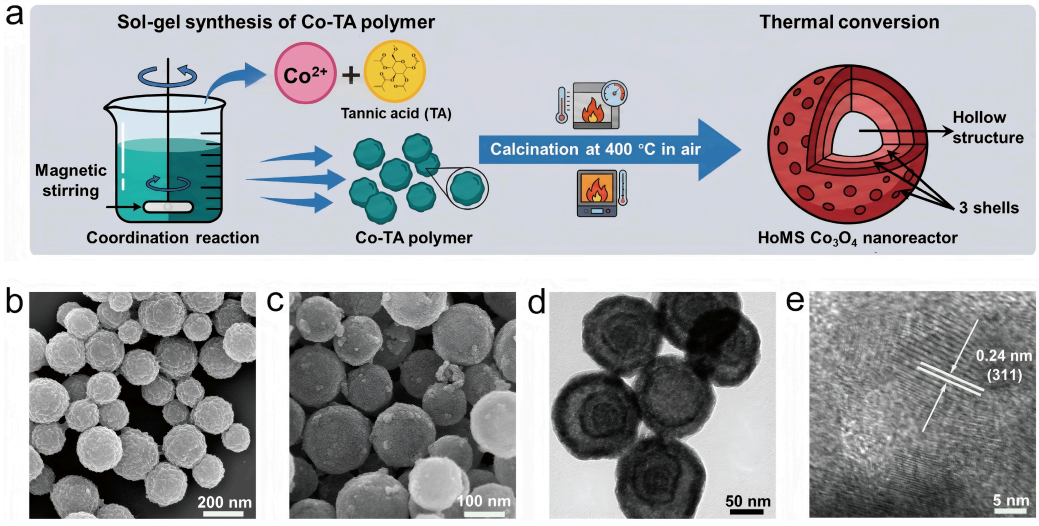


Figure 1. (**a**) Schematic illustration of the synthesis procedure for HoMS Co_3O_4 nanoreactors via a sol–gel method followed by thermal conversion. SEM images of (**b**) the Co-TA precursor and (**c**) the HoMS Co_3O_4 nanoreactors. (**d**) TEM image and (**e**) HR-TEM image of the HoMS Co_3O_4 nanoreactors.

The phase composition and crystal structure were further characterized by X-ray diffraction (XRD). As presented in Figure 2a, the HoMS Co_3O_4 nanoreactors display sharp and well-defined diffraction peaks at 2θ = 18.99°, 31.27°, 36.85°, 44.81°, 55.65°, 59.35° and 65.23°, which are indexed to the (111), (220), (311), (400), (422), (511) and (440) planes

of cubic spinel Co_3O_4 (JCPDS No. 74-2120) respectively [44,45]. No additional impurity peaks were observed, confirming the phase purity of the synthesized product. XPS was performed to probe the surface chemical composition and electronic states of the HoMS Co_3O_4. The high-resolution Co 2p spectrum (Figure 2b) was fitted with constraints on peak positions and FWHM based on the spinel Co_3O_4 structure [43]. The Co^{2+} $2p_{3/2}$ peak appears at 780.3 eV (FWHM = 2.1 eV), while the Co^{3+} $2p_{3/2}$ peak appears at 781.7 eV (FWHM = 2.3 eV), with satellite peaks at 805.2 eV. The Co^{2+}/Co^{3+} ratio was determined to be 1.30. The O 1s spectrum (Figure 2c) can be deconvoluted into three components, corresponding to lattice oxygen (O_{lat}), bridging hydroxyl groups (-OH) and adsorbed oxygen species respectively, indicating the presence of surface hydroxyl groups that may facilitate interfacial interactions with PDS [43–45]. The porous characteristics of the HoMS Co_3O_4 nanoreactors were evaluated by N_2 adsorption–desorption analysis. As depicted in Figure 2d, the isotherm exhibits a typical type-IV curve with a distinct H3-type hysteresis loop in the relative pressure (P/P_0) range of 0.6–1.0, indicative of a mesoporous structure [46]. The corresponding pore size distribution (inset of Figure 2d) reveals a mean pore diameter of approximately 5.7 nm, which primarily originates from the interparticle voids generated by the assembly of nanoscale Co_3O_4 crystallites. The BET specific surface area of the HoMS Co_3O_4 nanoreactors was determined to be 71.2 m^2 g^{-1}, substantially higher than that of conventional Co_3O_4 nanoparticles. Considering the high surface area and unique hierarchically hollow multi-shelled structure, the HoMS Co_3O_4 nanoreactors would be a good catalyst for PDS activation [19].

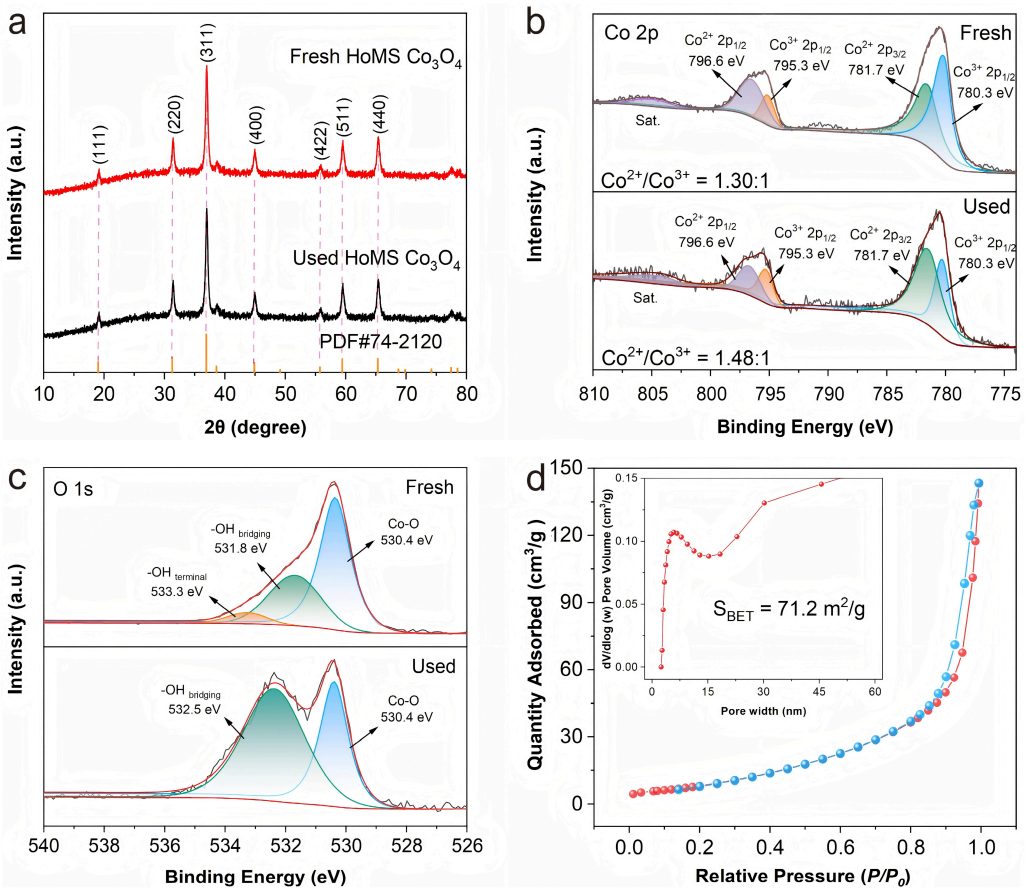


Figure 2. (**a**) XRD patterns, (**b**) high-resolution Co 2p XPS spectrum, (**c**) high-resolution O 1s XPS spectrum, and (**d**) N_2 adsorption–desorption isotherm with corresponding pore size distribution (inset) of the HoMS Co_3O_4 nanoreactors.

2.2. Catalytic Performance of HoMS Co_3O_4 Toward EOC Degradation

The catalytic performance of the HoMS Co_3O_4 nanoreactor was evaluated using BPA as a model pollutant. As shown in Figure 3a, the HoMS Co_3O_4 nanoreactor alone exhibited limited adsorption capacity, removing only approximately 7% of BPA within 90 min. Meanwhile, PDS alone, owing to its moderate redox potential (E_0 = 2.01 V), was incapable of effectively oxidizing BPA. In contrast, the HoMS Co_3O_4/PDS system achieved complete BPA removal within the same amount of time. The degradation kinetics of BPA were well described by a pseudo-first-order model with an apparent rate constant of 0.045 min^{-1}, which is competitive with most reported Co_3O_4-based catalysts (0.034–0.22 min^{-1}, Table S2). Inductively coupled plasma optical emission spectrometry (ICP-OES) analysis revealed a leached Co^{2+} concentration of 0.55 mg L^{-1} after the reaction, which is below the limit specified in the Chinese National Standard for Surface Water Quality (GB 3838-2002, 1.0 mg L^{-1}) [47], suggesting satisfactory structural stability of the HoMS Co_3O_4 nanoreactor. Homogeneous control experiments demonstrated that the leached Co^{2+} contributed to merely ~3% of BPA removal, confirming that the degradation predominantly proceeded via a heterogeneous catalytic pathway.

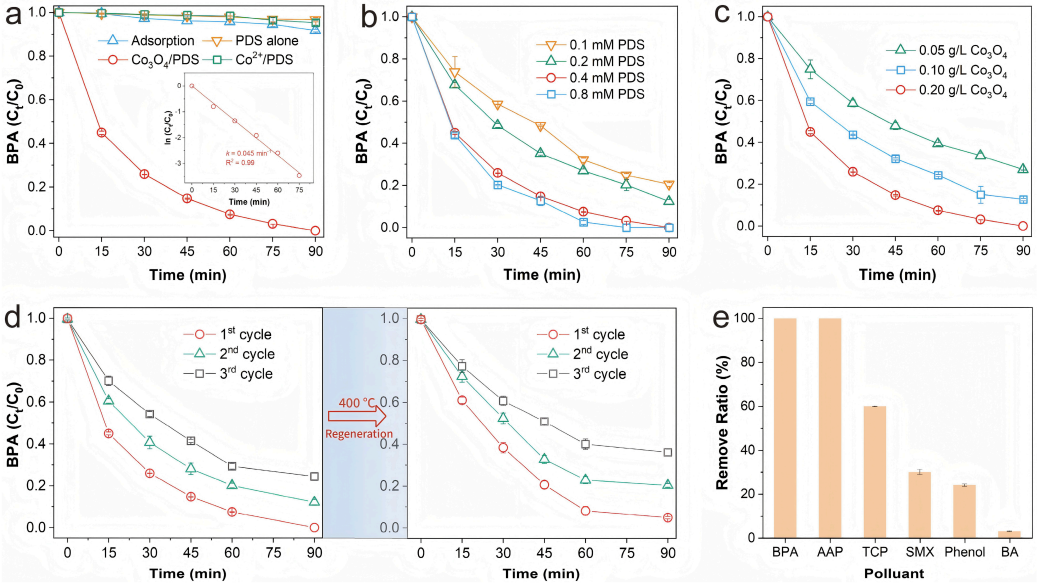


Figure 3. (**a**) Removal of BPA in different reaction systems and the corresponding kinetic plots in the HoMS Co_3O_4/PDS system. Effects of (**b**) HoMS Co_3O_4 dosage and (**c**) PDS concentration on BPA removal. (**d**) Reusability of the HoMS Co_3O_4 nanoreactor for BPA removal in consecutive runs. (**e**) Removal efficiencies of AAP, TCP, SMX, PhOH and BA in the HoMS Co_3O_4/PDS system under identical conditions. Reaction conditions: [pollutant] = 0.04 mM, [PDS] = 0.4 mM, [Co_3O_4] = 0.1 g L^{-1}, initial pH = 7.0 ± 0.2, T = 25 ± 0.3 °C.

To quantitatively assess the structural advantage of the HoMS architecture, we synthesized Co_3O_4 nanoparticles (Co_3O_4 NPs, Figure S1; detailed synthesis procedure described in Text S1) as a control catalyst. Under identical reaction conditions, Co_3O_4 NPs achieved only 49.5% BPA removal within 90 min (k_{obs} = 0.009 min^{-1}) (Figure S3a,b), substantially lower than the complete removal achieved by HoMS Co_3O_4 (k_{obs} = 0.045 min^{-1}). After normalizing the observed rate constants by the BET surface area (25.8 m^2 g^{-1} for Co_3O_4 NPs, 71.2 m^2 g^{-1} for HoMS Co_3O_4), the HoMS Co_3O_4 still exhibited a 1.85-fold higher normalized rate constant (6.3 × 10^{-4} min^{-1}·m^{-2}·g) compared to Co_3O_4 NPs (3.5 × 10^{-4} min^{-1}·m^{-2}·g) (Figure S3c,d). This confirms that the enhanced catalytic performance originates not merely from increased surface area but from the unique hollow multi-shelled

architecture itself, which induces a nanoconfinement effect that enriches local reactant concentrations, as we have previously demonstrated [19].

Both the HoMS Co_3O_4 dosage (Figure 3b) and PDS concentration (Figure 3c) positively influenced BPA removal. This enhancement is attributable to the increased availability of active sites and reactive species, respectively. Interestingly, further increasing the PDS concentration from 0.4 to 0.8 mM did not yield a corresponding improvement in BPA removal (Figure 3c). This plateau effect is plausibly ascribed to the saturation of accessible inner-sphere adsorption sites on the HoMS Co_3O_4 surface, a phenomenon commonly observed in surface-mediated electron-transfer processes where the number of available binding sites for PDS becomes rate-limiting [48–50]. The HoMS Co_3O_4 nanoreactor also exhibited good reusability. As shown in Figure 3d, the BPA removal efficiency remained above 70% after three consecutive cycles. The gradual loss of catalytic activity is attributed to the deposition of transformation intermediates on the catalyst surface, as previously reported in our studies and related literature [19,50]. Notably, calcination at 400 °C effectively decomposes these deposited intermediates, thereby restoring the accessible active sites and catalytic activity. Meanwhile, no significant morphological change or agglomeration of the HoMS Co_3O_4 nanoreactors was observed after regeneration, further contributing to the excellent stability (Figure S2b). The regenerated catalyst maintained stable performance with a BPA removal efficiency of approximately 60% after three additional cycles.

To assess the versatility of this system, the removal of various emerging organic contaminants with different molecular structures was investigated. As depicted in Figure 3e, the HoMS Co_3O_4/PDS system exhibited marked efficacy toward electron-rich pollutants, including acetaminophen (AAP, 99.9%), 2,4,6-trichlorophenol (TCP, 58.6%), sulfamethoxazole (SMX, 29.8%), and phenol (PhOH, 23.7%), under identical conditions. The significantly higher removal efficiency of BPA (100%) compared to phenol (23.7%) under identical conditions can be attributed to their different electron densities. BPA possesses two phenolic rings connected by a propylene bridge, providing higher electron density and more electron-rich sites for electron abstraction, which is the key step in the electron-transfer non-radical mechanism [51–53]. Notably, benzoic acid (BA) remained intact under the same reaction conditions, indicating that the oxidation process is highly selective. BA is widely employed as a chemical probe for $SO_4^{\bullet-}$ and $^{\bullet}OH$ [17]. Its recalcitrance to degradation thus verifies that the HoMS Co_3O_4/PDS system operates via a non-radical oxidation pathway.

2.3. Identification of ROS in the HoMS Co_3O_4/PDS System

To unravel the removal mechanism of organics in the HoMS Co_3O_4/PDS system, EPR spectroscopy and chemical quenching experiments were conducted to identify the potential involvement of reactive oxygen species (ROS). As depicted in Figure 4a, no characteristic signals attributable to DMPO-$SO_4^{\bullet-}$, DMPO-$^{\bullet}OH$, or TEMP-$^1O_2$ were detected in the HoMS Co_3O_4/PDS system, preliminarily excluding the participation of $SO_4^{\bullet-}$, $^{\bullet}OH$ or $^1O_2$ [54,55]. This inference was further corroborated by quenching experiments. As shown in Figure 4b, the addition of high-concentration (up to 1000 mM) MeOH and TBA, which are both efficient scavengers of $SO_4^{\bullet-}$ and $^{\bullet}OH$, exerted negligible inhibition on BPA removal. Likewise, L-histidine, a typical quencher for $^1O_2$, did not appreciably affect BPA removal (Figure 4c). Collectively, these results conclusively demonstrate that the oxidative transformation of organic contaminants is not governed by conventional ROS pathways [56,57].

Given the exclusion of radical-based mechanisms, investigation of the electron-transfer (ET) process, which has been increasingly recognized as a pivotal non-radical route in metal oxide-mediated PDS activation systems, was conducted. Potassium chromate (K_2CrO_4), which is a well-established electron-transfer inhibitor [58], was introduced into the reaction

system. As shown in Figure 4d, the addition of 10 mM K_2CrO_4 dramatically suppressed BPA removal, with the removal efficiency decreasing by approximately 70% and the corresponding pseudo-first-order rate constant plummeting from 0.0791 to 0.0035 min^{-1} (Figure S4). Such pronounced inhibition indicates that the electron-transfer (ET) regime, a widely recognized non-radical process, dominates the oxidation of BPA in the HoMS Co_3O_4/PDS system.

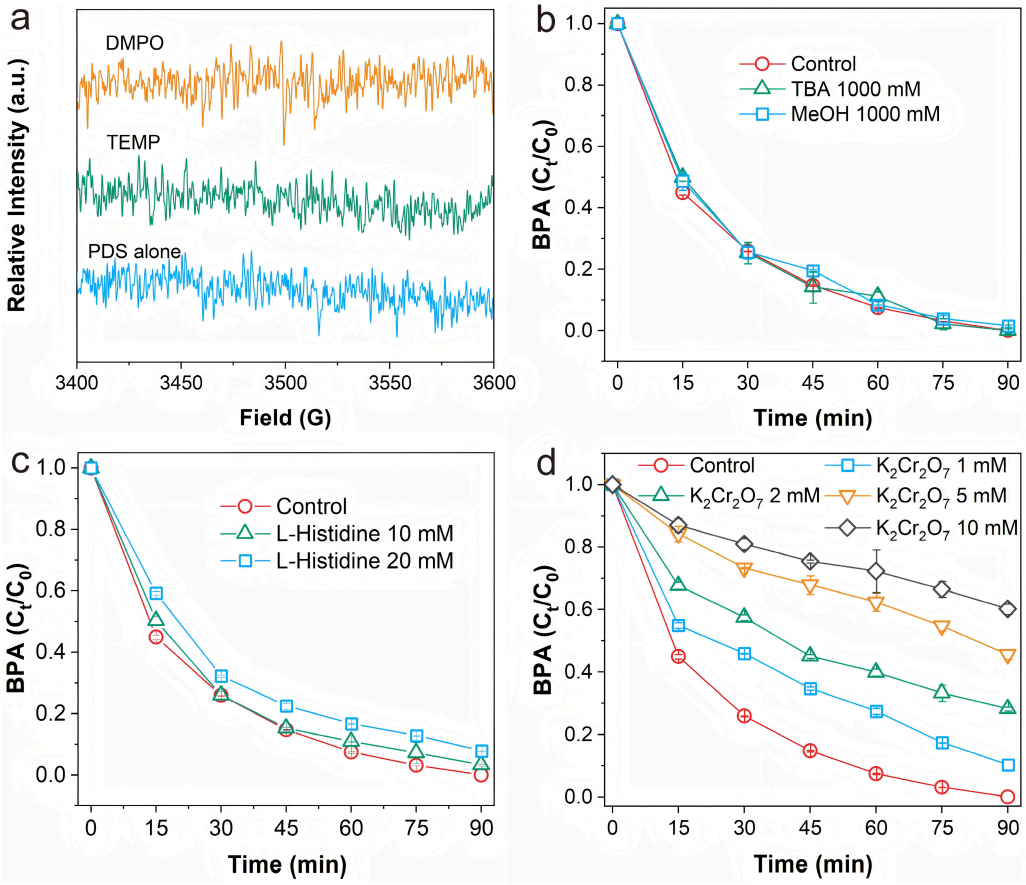


Figure 4. (**a**) EPR spectra of $SO_4^{\bullet-}$/$^{\bullet}$OH and $^1O_2$ using DMPO and TEMP as spin-trapping agents, respectively. Effects of (**b**) MeOH and TBA, (**c**) L-histidine and (**d**) K_2CrO_4 as quenchers on BPA removal. Reaction conditions: [BPA] = 0.04 mM, [PDS] = 0.4 mM, [Co_3O_4] = 0.1 g L^{-1}, initial pH = 7.0 ± 0.2, T = 25 ± 0.3 °C.

2.4. Verification of the Electron-Transfer Mechanism

To verify the proposed ET mechanism, electrochemical measurements were performed using a HoMS Co_3O_4-modified electrode. The chronoamperometric (I-t) response (Figure 5a) revealed a distinct anodic current upon the injection of PDS at 200 s, indicating facile electron migration from the electrode surface to the adsorbed PDS molecules. Notably, a subsequent addition of BPA (1 mM) at 600 s triggered an additional current spike, the intensity of which increased proportionally with BPA concentration, providing strong evidence that BPA serves as an electron donor to the surface-bound PDS species [58,59]. Complementary evidence was provided by the decomposition behavior of PDS. As shown in Figure 5b, PDS exhibited negligible self-decomposition in aqueous solution. When HoMS Co_3O_4 was present, approximately 50% of PDS was decomposed within 90 min. More importantly, the introduction of BPA significantly accelerated PDS consumption. The decomposition efficiency of PDS increased to 66% with 0.04 mM BPA and further to 75% with 0.08 mM BPA. This concentration-dependent acceleration indicates that the surface-

complexed PDS directly extracts electrons from BPA [58], thereby driving simultaneous oxidant depletion and substrate oxidation.

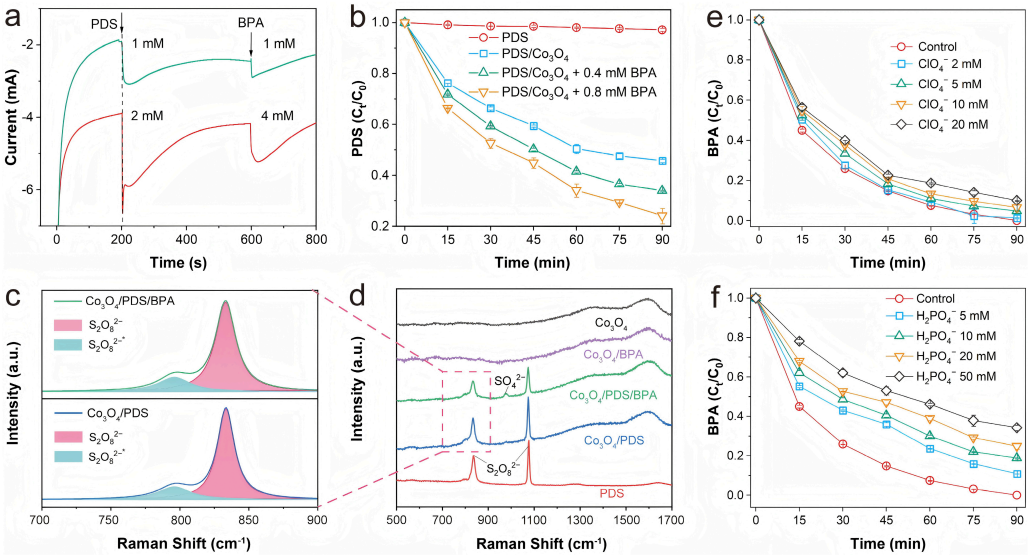


Figure 5. (**a**) Current-time (i-t) curves of the HoMS Co_3O_4 electrode under different reaction conditions. (**b**) Decomposition behaviors of PDS in the absence and presence of HoMS Co_3O_4 and BPA. (**c**) In situ Raman spectra of PDS, HoMS Co_3O_4/PDS, HoMS Co_3O_4/PDS/BPA, Co_3O_4/BPA and Co_3O_4. (**d**) High-resolution Raman spectrum of the surface-complexed PDS species (denoted as PDS*). Effect of (**e**) ClO_4^- and (**f**) HPO_4^{2-} on BPA removal. Reaction conditions: [BPA] = 0.04 mM, [PDS] = 0.4 mM, [Co_3O_4] = 0.1 g L^{-1}, initial pH = 7.0 ± 0.2, T = 25 ± 0.3 °C.

To confirm the formation of the surface-complexed PDS species, in situ Raman spectroscopy was performed. As shown in Figure 5c,d, pristine PDS exhibits characteristic vibrational bands at 835 cm^{-1} and 1075 cm^{-1} [58,59]. After the addition of HoMS Co_3O_4, a new Raman peak at 796 cm^{-1} emerges, which is characteristic of a surface-complexed PDS species (denoted as PDS*) formed through adsorption without O-O bond cleavage [60–62]. The assignment of the 796 cm^{-1} Raman peak to surface-complexed PDS* is supported by reference spectra and literature reports. Ren et al. [60] identified this peak at approximately 796 cm^{-1} as characteristic of surface-activated PDS* on carbon nanotubes during electron-transfer-mediated non-radical oxidation. This assignment has been widely adopted in subsequent studies on electron-transfer regimes in persulfate activation [61,62]. In our previous work on Ce-doped CuO/PDS systems, we also observed the same Raman feature at 796 cm^{-1}, confirming the presence of PDS* as the dominant reactive intermediate [17]. Therefore, the Raman data presented in this study are consistent with these established literature reports and provide strong evidence for the formation of PDS* on the HoMS Co_3O_4 surface. Upon subsequent addition of BPA, the intensity of the PDS peaks progressively diminishes, while a new signal at 981 cm^{-1} (attributed to SO_4^{2-}) appears. This spectral evolution suggests that the surface-complexed PDS serves as the electron acceptor and is consumed during the oxidative transformation of BPA, further corroborating the proposed electron-transfer pathway. The interfacial interaction between PDS and the HoMS Co_3O_4 nanoreactors was further probed by in situ FT-IR spectroscopy (Figure S5). The FT-IR spectrum of pristine PDS exhibits characteristic bands at 1050 cm^{-1} and 1272 cm^{-1}, corresponding to the symmetric stretching vibrations of S=O=S and S-O-S, respectively [7,58]. Upon mixing with HoMS Co_3O_4, these peaks remain unshifted and no additional bands emerge. When BPA is introduced into the HoMS Co_3O_4/PDS mixture, a new absorption band appears at 1107 cm^{-1}, which is assignable to SO_4^{2-}, evidencing that electron donation from BPA triggers the decomposition of the surface-bound PDS into sulfate.

2.5. Interfacial Interaction and PDS Activation Mechanism

To further discern the interaction between PDS and HoMS Co_3O_4 nanoreactors, the influence of ionic strength on BPA removal was examined. As shown in Figure 5e, the addition of perchlorate (ClO_4^-, 2–20 mM), a typical non-coordinating anion [63,64], exerted negligible effect on BPA degradation. This insensitivity to ionic strength strongly suggests that PDS binding on the HoMS Co_3O_4 surface proceeds via an inner-sphere complexation mechanism, rather than outer-sphere electrostatic association. In contrast, the introduction of hydrogen phosphate (HPO_4^{2-}) resulted in a pronounced inhibition of BPA removal (Figure 5f). HPO_4^{2-} is known to possess a strong affinity for surface hydroxyl groups (-OH) on metal oxides, and thus competitively occupies the same coordination sites that are essential for PDS adsorption [63]. This marked inhibitory effect confirms that surface hydroxyl groups (-OH) play a critical role in anchoring PDS onto the HoMS Co_3O_4 surface to form the reactive surface complex. This assignment is further supported by XPS analysis (Figure 2c), which reveals a decrease in surface -OH and a concurrent increase in bridging -OH after the catalytic reaction, corroborating the participation of surface -OH in the formation of the PDS complex and the ensuing electron-transfer oxidation.

On the basis of the above spectroscopic and competitive adsorption evidence, a mechanistic scheme for PDS activation over the HoMS Co_3O_4 nanoreactors is proposed (Figure 6). PDS molecules are first anchored onto the HoMS Co_3O_4 surface through inner-sphere coordination with surface metal sites (most plausibly via Co-O-S interactions), without involving covalent O-O bond scission. This surface complexation elongates the O-O bond and polarizes the peroxide linkage, generating a surface-bound PDS species with an enhanced oxidizing capability (Step I). This activated complex then functions as an electron-transfer bridge upon encountering electron-rich organic pollutants (e.g., BPA). It directly abstracts electrons from the contaminants, leading to concurrent PDS decomposition (to SO_4^{2-}) and oxidative degradation of the organics via a non-radical pathway (Step II). The hollow multi-shelled architecture further amplifies this process by providing abundant accessible active sites and enriching local reactant concentrations through the nanoconfinement effect, thereby boosting the overall catalytic efficiency.

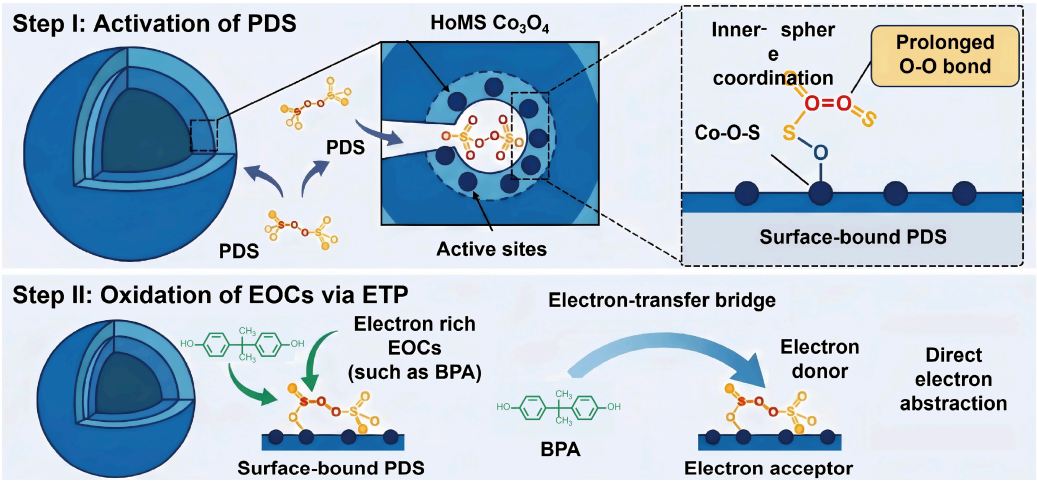


Figure 6. Schematic illustration of the proposed mechanism for PDS activation and subsequent electron-transfer oxidation of organic contaminants over the HoMS Co_3O_4 nanoreactors.

2.6. Degradation Pathway of BPA in the HoMS Co_3O_4/PDS System

Total organic carbon (TOC) analysis revealed that the removal efficiency after 90 min of reaction was approximately 45.2%, indicating that BPA was not completely mineralized and transformation intermediates were generated during the reaction. A total of eight interme-

diates were detected by liquid chromatography–mass spectrometry (LC-MS) measurements (Table S3). Based on these identified intermediates and relevant literature reports [19,58], a plausible degradation pathway for BPA in the HoMS Co_3O_4/PDS system is proposed. As shown in Figure S6, hydroxylation, ketonization and oxidative ring-opening reactions are involved in the transformation pathways. In the hydroxylation pathway, BPA is initially converted to monohydroxylated BPA (TP1, m/z = 244), which subsequently undergoes dehydrogenation to form a quinone-type intermediate (TP2, m/z = 242). This quinone intermediate is then oxidized to a carboxylic acid derivative (TP3, m/z = 277). In the electron-transfer pathway, the O-H bond of BPA is preferentially attacked, consistent with the non-radical degradation mechanism [58], generating a BPA radical intermediate (TP4, m/z = 227). This radical rapidly converts to a quinone-type carbon radical (TP5, m/z = 227), followed by β-scission to yield intermediate 6 (TP6, m/z = 97). These intermediates are subsequently transformed via ring-opening reactions to small molecular TP7 (m/z = 100) and TP8 (m/z = 114), which are ultimately decomposed into CO_2 and H_2O.

2.7. Practical Applicability and Long-Term Stability of the HoMS Co_3O_4/PDS System

Non-radical oxidation systems are intrinsically characterized by mild redox potentials, broad pH adaptability, and robust resistance to coexisting water constituents [16,65]. As illustrated in Figure 7a, the HoMS Co_3O_4/PDS system maintained highly efficient BPA removal across a wide initial pH range (3–11), with negligible variation compared to that at pH 7, confirming its excellent pH tolerance. The influence of common inorganic anions and natural organic matter was further evaluated (Figure 7b,c). Notably, the presence of Cl^- (5.0–50.0 mM), SO_4^{2-} (5.0 mM), NO_3^- (5.0 mM), CO_3^{2-} (5.0 mM), and humic acid (HA, 5 mg/L) did not appreciably suppress BPA removal. This marked anti-interference capability stands in stark contrast to conventional radical-based persulfate systems, where these background species aggressively scavenge reactive radicals (e.g., $SO_4^{\bullet-}$ and $^{\bullet}OH$), thereby severely compromising oxidative efficiency [66,67]. The exceptional selectivity of the present system is fundamentally ascribed to its electron-transfer non-radical pathway, which circumvents such non-specific consumption of reactive species and ensures that the oxidative capacity is exclusively directed toward target organic pollutants.

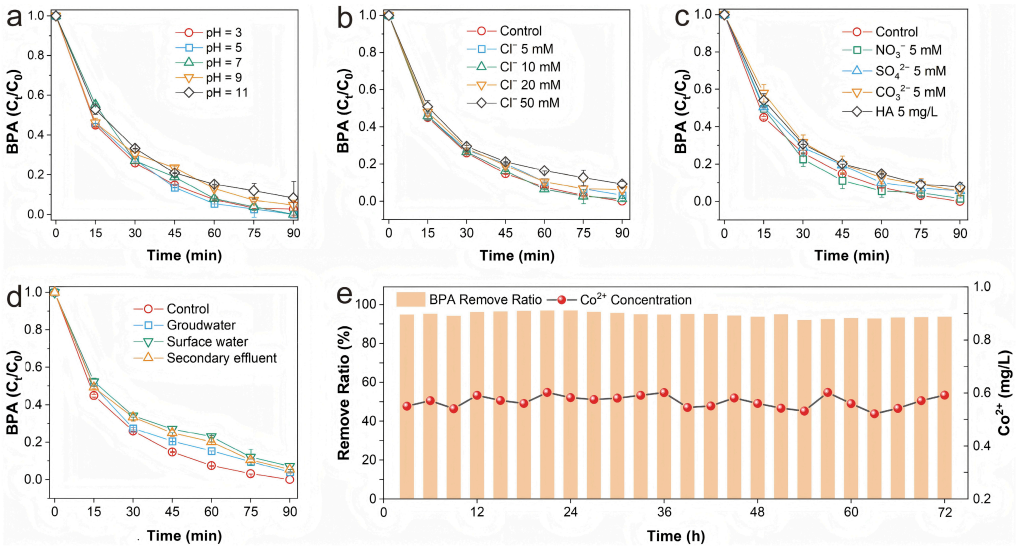


Figure 7. (**a**) Effect of initial pH on BPA removal in the HoMS Co_3O_4/PDS system. (**b**) Influence of Cl^- and (**c**) other common background constituents (NO_3^-, SO_4^{2-}, CO_3^{2-} and HA) on BPA removal. (**d**) BPA removal efficiencies in surface water, groundwater, and secondary effluent from a municipal wastewater treatment plant. (**e**) BPA removal performance in a continuous flow-through reactor over 72 h of operation and corresponding Co^{2+} leaching concentration.

Given this robust performance under diverse backgrounds, the HoMS Co_3O_4/PDS system was further challenged with real water matrices. As depicted in Figure 7d, BPA removal efficiencies in surface water, groundwater, and secondary effluent from a municipal wastewater treatment plant reached 95.3%, 94.7% and 93.2% respectively under identical reaction conditions. The slightly lower efficiency in the secondary effluent is likely attributable to the competitive adsorption of coexisting organic matter on the catalyst surface, which marginally reduces the availability of active sites for PDS activation [19,58]. Nevertheless, these results underscore the system's robustness and its potential for on-site remediation applications.

To further assess the practical applicability of the HoMS Co_3O_4 nanoreactor, a continuous flow-through reactor was constructed by packing 0.5 g of the catalyst with 2.0 g of quartz sand (0.2–0.5 mm) in a glass column (10 mm inner diameter × 150 mm length), yielding a catalyst packing density of 0.42 g cm^{-3} and a bed volume of 5.95 cm^3. At a flow rate of 1.0 mL min^{-1}, the hydraulic retention time was 4.6 min, and the pressure drop across the column remained below 0.5 kPa throughout 72 h of continuous operation, indicating negligible hydraulic resistance. As shown in Figure 7e, the BPA removal efficiency remained consistently above 90% over the entire operation period, while the leached Co^{2+} concentration remained below the limit specified in the Chinese national standard (GB 3838-2002, 1.0 mg L^{-1}), confirming the environmental safety and structural integrity of the catalyst. Moreover, the spent catalyst could be readily regenerated by in situ calcination at 400 °C (Figure 3d), and the regenerated column maintained stable performance. These results, together with the use of commercially available packing materials and the simple column configuration, demonstrate the potential for practical scale-up, while further optimization of catalyst shaping and reactor design would be needed for full-scale implementation. Considering the good catalytic performance, cost-effective synthesis from earth-abundant precursors (tannic acid and cobalt salts), and robust long-term stability, the HoMS Co_3O_4 nanoreactor represents a good candidate for the selective remediation of water contaminated with electron-rich emerging organic pollutants.

3. Materials and Methods

3.1. Chemicals

Tannic acid (TA, ≥98%), cobalt nitrate hexahydrate $Co(NO_3)_2{\cdot}6H_2O$, poly(ethylene oxide)-poly(propylene oxide) (F127, average Mw~12,600), formaldehyde (CH_2O, 37 wt% in water), ammonia water ($NH_3{\cdot}H_2O$, 25–28 wt%), sodium persulfate ($Na_2S_2O_8$, PDS), bisphenol A (BPA), sulfamethoxazole (SMX), hydrochloric acid (HCl, 37 wt%), tert-butyl alcohol (TBA), benzoquinone (BQ), Methanol (MeOH), and 5,5-dimethyl-1-pyrroline N-oxide (DMPO) were purchased from Macklin Biochemical Co., Ltd. (Shanghai, China). All reagents were of analytical grade and used as received without further purification. Ultrapure water (resistivity >18.2 MΩ·cm) was used throughout all experiments.

3.2. Synthesis of HoMS Co_3O_4 Nanoreactors

The hollow multi-shelled Co_3O_4 nanospheres (HoMS Co_3O_4) were synthesized via a sol–gel method followed by thermal conversion. Briefly, the coordination polymer of Co^{2+} and TA was first prepared according to a previously reported sol–gel procedure. The detailed synthesis parameters are provided in Text S1 of the Supporting Information (SI). The as-obtained Co-TA polymer was then subjected to calcination in a muffle furnace at 400 °C for 2 h in air with a ramping rate of 5 °C min^{-1}, yielding the HoMS Co_3O_4 nanoreactors. Co_3O_4 nanoparticles were also synthesized as a non-hollow control catalyst using a procedure similar to that of HoMS Co_3O_4, except that formaldehyde was omitted in the precursor preparation.

3.3. Characterizations

The morphology and microstructure of the as-synthesized HoMS Co_3O_4 were examined using field-emission scanning electron microscopy (SEM, Hitachi S-4800, Hitachinaka, Japan) at an accelerating voltage of 10 kV and transmission electron microscopy (TEM, FEI Tecnai G2 F20, Hillsboro, OR, USA) operated at 200 kV. Crystal structures were characterized by X-ray diffraction (XRD, Rigaku Ultimate IV, Tokyo, Japan) with Cu Kα radiation (λ = 1.5418 Å) operating at 40 kV and 40 mA. Diffraction patterns were recorded in the 2θ range of 10–80° with a scan rate of 2° min^{-1} and a step size of 0.02°. The specific surface area was determined by the Brunauer–Emmett–Teller (BET) method, and pore size distributions were calculated from the desorption branch using the Barrett–Joyner–Halenda (BJH) model, based on N_2 adsorption–desorption isotherms measured at 77 K on a TriStar II 3020 analyzer (Micromeritics, Norcross, GA, USA). Prior to analysis, all samples were degassed at 150 °C overnight under vacuum. Electrochemical measurements were conducted on a CHI660E electrochemical workstation (CH Instruments, Shanghai, China) using a conventional three-electrode system. A glassy carbon electrode (GCE, 3 mm diameter) coated with the HoMS Co_3O_4 catalyst served as the working electrode, a platinum wire as the counter electrode, and an Ag/AgCl (saturated KCl) electrode as the reference. All electrochemical tests were performed in 0.5 g L^{-1} Na_2SO_4 electrolyte (pH 7.0) at room temperature. In situ attenuated total reflectance Fourier-transform infrared spectroscopy (ATR-FTIR, Nicolet iS10, Thermo Fisher, Waltham, MA, USA) was employed to probe the interfacial interaction between HoMS Co_3O_4 and PDS. Spectra were recorded in the range of 400–2000 cm^{-1} with a resolution of 4 cm^{-1}. In situ Raman spectroscopy was performed on a Horiba HR Evolution laser confocal Raman spectrometer (Horiba, Palaiseau, France) equipped with a 532 nm excitation laser at a power of 0.08 mW to avoid sample heating. Raman spectra were collected in the range of 200–1500 cm^{-1} with an acquisition time of 10 s and 3 accumulations.

3.4. Catalytic Oxidation Experiments

Catalytic oxidation experiments were carried out in a 100 mL glass beaker at room temperature under magnetic stirring. In a typical run, 50 mg of HoMS Co_3O_4 catalyst was dispersed in 50 mL of an aqueous solution containing 10 mg L^{-1} of the target organic pollutant. The suspension was stirred for 30 min to establish adsorption–desorption equilibrium. Then, 0.5 mL of freshly prepared PDS stock solution (40 mM) was injected to yield an initial PDS concentration of 0.4 mM, initiating the catalytic reaction. The initial pH was adjusted to 7.0 ± 0.1 using 0.1 M HCl or 0.1 M NaOH as required. At predetermined time intervals, 1.0 mL aliquots were withdrawn and immediately filtered through a 0.22 μm polyethersulfone (PES) syringe filter to remove catalyst particles. The filtrate was quenched with 0.5 mL of methanol to terminate any residual radical reactions. All oxidation experiments were performed in duplicate, and the data are presented as mean values with standard deviations (error bars). The residual concentration of organic pollutants was determined by high-performance liquid chromatography (HPLC, Agilent 1220 Infinity LC, Santa Clara, CA, USA) equipped with a C18 reversed-phase column (4.6 × 150 mm). The column temperature was maintained at 30 °C, and the flow rate was 1.0 mL min^{-1}. The regeneration process involved collecting the spent catalyst by filtration, washing with ultrapure water and ethanol, drying at 60 °C for 12 h, and calcining at 400 °C for 2 h in air (ramping rate 5 °C min^{-1}).

3.5. Identification of Reactive Species

To identify the reactive oxygen species (ROS) involved in the HoMS Co_3O_4/PDS system, electron paramagnetic resonance (EPR) spectroscopy was performed on a Bruker

EMXmicro-6/1 spectrometer (Bruker, Rheinstetten, Germany). DMPO and TEMP (2,2,6,6-tetramethyl-4-piperidone) were used as spin-trapping agents for $SO_4^{\bullet-}$/$^{\bullet}OH$ and $^1O_2$, respectively. In a typical EPR test, the catalyst (1.0 g L^{-1}), PDS (0.4 mM), and the spin-trapping agent were mixed in 1 mL of ultrapure water. The mixture was transferred to a quartz capillary tube, and EPR spectra were recorded immediately (within 1 min) and after 10 min of reaction. The microwave frequency was 9.85 GHz, and the modulation frequency was 100 kHz.

4. Conclusions

In summary, hollow multi-shelled Co_3O_4 nanoreactors were successfully synthesized via a cost-effective self-templating strategy using plant-derived tannic acid. The unique hollow architecture provides abundant accessible active sites and enhanced nanoconfinement effects, enabling efficient PDS activation for EOC removal. Mechanistically, the HoMS Co_3O_4/PDS system operates through an electron-transfer-mediated non-radical pathway, wherein surface-complexed PDS* species with a polarized O-O bond directly abstract electrons from pollutants. This pathway confers high selectivity toward electron-rich contaminants, broad pH adaptability (3–11), strong resistance to coexisting water constituents, and robust performance in real water matrices (>93% BPA removal). Moreover, the system maintains stable operation in a continuous flow-through reactor over 72 h with negligible Co^{2+} leaching. The study provides a viable and sustainable strategy for the selective remediation of electron-rich EOCs, offering a promising alternative to conventional radical-based oxidation processes that suffer from poor selectivity and matrix interference.

Supplementary Materials: The following supporting information can be downloaded at: https://www.mdpi.com/article/10.3390/catal16090754/s1, Figure S1: SEM image of Co_3O_4 NPs; Figure S2: SEM images of HoMS Co_3O_4 (a) before and (b) after calcination regeneration. (c) Particle size distribution of HoMS Co_3O_4 determined by statistical analysis of SEM images. (d) HR-TEM image of another HoMS Co_3O_4 nanoreactor; Figure S3: (a) BPA removal efficiency and (b) corresponding pseudo-first-order kinetic plots in the HoMS Co_3O_4/PDS and Co_3O_4 NPs/PDS systems. (c) N_2 adsorption-desorption isotherm of the Co_3O_4 nanoparticles. (d) Normalized rate constants (k/S_{BET}) for BPA degradation in both systems; Figure S4: Kinetic rates of BPA removal with different concentrations of K_2CrO_4. Reaction conditions: [BPA] = 0.04 mM, [PDS] = 0.4 mM, [Co_3O_4] = 0.1 g L^{-1}, initial pH = 7.0 ± 0.2, T = 25 ± 0.3 °C; Figure S5: In situ ATR-FTIR spectra of pristine PDS, HoMS Co_3O_4/PDS, and HoMS Co_3O_4/PDS/BPA systems; Figure S6: Proposed degradation pathways of BPA in the HoMS Co_3O_4/PDS system; Table S1: The mobile phase and detection wavelength for each contaminant; Table S2: Comparison of catalytic performance for various Co-based catalysts in persulfate activation for organic pollutant degradation; Table S3. Identified reaction intermediates of BPA in the HoMS Co_3O_4/PDS system. Text S1: Synthesis of Co-TA polymer and HoMS Co_3O_4. References [68–72] are cited in the Supplementary Materials.

Author Contributions: Formal analysis, Writing—Original draft preparation, Y.W.; Investigation, Y.P.; Visualization, C.Z.; Writing—review and editing, G.W.; Writing—review and editing, Funding acquisition, P.J. All authors have read and agreed to the published version of the manuscript.

Funding: This research was funded by the National Natural Science Foundation of China (No. 52230001).

Data Availability Statement: The datasets generated and analyzed during the current study are available from the corresponding author upon reasonable request.

Acknowledgments: The authors appreciate the help from Shaanxi Key Laboratory of Environmental Engineering.

Conflicts of Interest: The authors declare no conflicts of interest.

Abbreviations

The following abbreviations are used in this manuscript:

HoMS	Hollow multi-shelled structure
EOCs	Emerging organic contaminants
PS-AOPs	Persulfate-based advanced oxidation processes
ROS	Reactive oxygen species
TA	Tannic acid
PDS	Peroxydisulfate
BPA	Bisphenol A
TCP	2,4,6-Trichlorophenol
SMX	Sulfamethoxazole
AAP	Acetaminophen
BA	Benzoic acid
BQ	Benzoquinone
MeOH	Methanol
TBA	tert-Butyl alcohol
TEMP	2,2,6,6-Tetramethyl-4-piperidone
DMPO	5,5-Dimethyl-1-pyrroline N-oxide
SEM	Scanning electron microscopy
TEM	Transmission electron microscopy
XRD	X-ray diffraction
HR-TEM	High-resolution transmission electron microscopy
ATR-FTIR	Attenuated total reflectance Fourier-transform infrared spectroscopy
ETP	Electron-transfer process
TOC	Total organic carbon
LC-MS	Liquid chromatography–mass spectrometry

References

1. Peng, F.J.; Feng, X.J.; Li, S.; Yu, X.L.; Chen, J.; Liu, S.S.; Ying, G.G.; Liu, Y.S. Removal of Emerging Organic Contaminants in a Subsurface Wastewater Infiltration System: A Preliminary Study of Microbial Mechanism. *Water Res.* **2025**, *284*, 123960. [CrossRef] [PubMed]
2. Tisler, S.; Kilpinen, K.; Devers, J.; Castro, M.; Jorgensen, M.B.; Mandava, G.; Lundqvist, J.; Cedergreen, N.; Christensen, J.H. Mapping Emerging Contaminants in Wastewater Effluents Through Multichromatographic Platform Analysis and Source Correlations. *Environ. Sci. Technol.* **2025**, *59*, 5766–5774. [CrossRef] [PubMed]
3. Wang, A.G.; Wu, W.M.; Dong, M.D.; Ji, M.; Yu, Z.Q.; Liang, Y.X.; Xu, M.Y. Making Waves: Harnessing Electroactive Microorganisms for Efficient and Sustainable Removal of Emerging Contaminants in Wastewater Treatment Plants. *Water Res.* **2026**, *289*, 124900. [CrossRef] [PubMed]
4. Li, S.; Wang, H.; Xu, H.; Pei, H. Investigation of Nitro(So)- and Chloro-Disinfection Byproduct Formation Mechanisms After UV/Cl_2 and UV/H_2O_2 Oxidation of 2-Methylisoborneol in the Presence of Algal Organic Matter. *Water Res.* **2026**, *288*, 124616. [CrossRef] [PubMed]
5. Zhang, X.; Nan, J.; Zhang, H.; Lin, Z.; Chai, H.; Song, L.; Cheng, Y. Dual-Engineered $MoSe_2$/TNC for Energy-Efficient Degradation of Diverse Contaminants in PEC-PMS Systems: Mechanism and Lifecycle Assessment. *Appl. Catal. B* **2026**, *390*, 126641. [CrossRef]
6. Yu, G.; Zhao, W.; Wei, H.; Li, S.; Yang, F.; Wang, X.; Zhuang, C.; Zhang, J.; Zhan, S. Bridge-Bonded Mn-O-Mn Interfaces Decouple PMS Adsorption from Activation Toward Singlet-Oxygen-Selective Water Decontamination. *Appl. Catal. B* **2026**, *399*, 127100. [CrossRef]
7. Wang, G.; An, W.; Zhang, Y.; Liu, Z.; Yang, S.; Jin, P.; Ding, D. Mesoporous Carbon Framework Supported Cu-Fe Oxides as Efficient Peroxymonosulfate Catalyst for Sustained Water Remediation. *Chem. Eng. J.* **2022**, *430*, 133060. [CrossRef]
8. Qian, J.; Ma, R.; Chen, Z.; Wang, G.; Zhang, Y.; Du, Y.; Chen, Y.; An, T.; Ni, B.J. Hierarchical Co-Fe Layered Double Hydroxides (LDH)/Ni Foam Composite as a Recyclable Peroxymonosulfate Activator Towards Monomethylhydrazine Degradation: Enhanced Electron Transfer and $^1O_2$ Dominated Non-Radical Pathway. *Chem. Eng. J.* **2023**, *469*, 143554. [CrossRef]
9. Xu, X.; Zhang, S.; Wang, Y.; Lin, Y.; Guan, Q.; Chen, C. Identifying the Role of Surface Hydroxyl on FeOCl in Bridging Electron Transfer Toward Efficient Persulfate Activation. *Environ. Sci. Technol.* **2023**, *57*, 12922–12930. [CrossRef] [PubMed]

10. Zhao, X.; Zhang, Z. Heterogeneous Peroxymonosulfate-Based Advanced Oxidation Mechanisms: New Wine in Old Bottles? *Environ. Sci. Technol.* **2025**, *59*, 5913–5924. [CrossRef] [PubMed]
11. Wang, G.; Zhang, Y.; Ge, L.; Liu, Z.; Zhu, X.; Yang, S.; Jin, P.; Zeng, X.; Zhang, X. Monodispersed CuO Nanoparticles Supported on Mineral Substrates for Groundwater Remediation Via a Nonradical Pathway. *J. Hazard. Mater.* **2022**, *429*, 128282. [CrossRef] [PubMed]
12. Hu, X.; Zhu, M. Were Persulfate-Based Advanced Oxidation Processes Really Understood? Basic Concepts, Cognitive Biases, and Experimental Details. *Environ. Sci. Technol.* **2024**, *58*, 10415–10444. [CrossRef] [PubMed]
13. Wang, M.M.; Liu, P.X.; Ye, F.; Liu, L.J.; Wen, J.T.; Ni, B.J.; Luo, H.W.; Wang, W.K.; Xu, J. 2D Ni-Co Bimetallic Oxide Nanosheets Activate Persulfate for Targeted Conversion of Bisphenol A in Wastewater Into Polymers. *Environ. Int.* **2024**, *184*, 108466. [CrossRef] [PubMed]
14. Liu, Y.Q.; Tian, L.; Huang, M.; Liu, H.Z.; Guo, Z.Y.; Ding, J.; Xia, W.Q.; Teng, L.; Yu, H.Q.; Li, W.W. Magnesium Oxide-Supported Single Atoms with Fine-Modulated Steric Location for Polymerization Transfer Removal of Water Pollutants. *Environ. Sci. Technol.* **2025**, *59*, 880–891. [CrossRef] [PubMed]
15. Wu, B.; Li, Z.L.; Zhang, J.; Zhou, W.Y.; Ho, S.H.; Duan, X.G.; Wang, A.J. Axially Engineered Single Atoms in Enzyme-Mimic-Binding Pocket Steering Dehalogenation-Polymerization Pathways Toward Water Pollutant Upcycling. *Nat. Commun.* **2026**, *17*, 12345. [CrossRef] [PubMed]
16. Ren, W.; Cheng, C.; Shao, P.; Luo, X.; Zhang, H.; Wang, S.; Duan, X. Origins of Electron-Transfer Regime in Persulfate-Based Nonradical Oxidation Processes. *Environ. Sci. Technol.* **2022**, *56*, 78–97. [CrossRef] [PubMed]
17. Xie, W.J.; Wang, Z.X.; Yin, Y.F.; Bai, Y.B.; Yang, J.Q.; Miao, D.L.; Zeng, X.K.; Yang, S.J.; Wang, G. Selective Polymerization of Chlorophenols in Hypersaline Wastewater Via Surface-Complex-Mediated Electron Transfer Over Ce-Doped CuO. *Water Res.* **2025**, *284*, 124023. [CrossRef] [PubMed]
18. Wang, Z.; Yin, Y.; Yang, J.; Duan, J.; Zeng, X.; Ren, W.; Yang, S.; Wang, G. Electron Transfer-Driven Polymerization of Phenolics Via CuO-Catalyzed Peracetic Acid for Sustainable Wastewater Remediation. *J. Hazard. Mater.* **2026**, *501*, 140680. [CrossRef] [PubMed]
19. Wang, G.; Wang, K.; Liu, Z.; Feng, Y.; Yang, S.; Su, Y.; Qian, X.; Jin, P.; Wei, J. Hollow Multi-Shelled NiO Nanoreactor for Nanoconfined Catalytic Degradation of Organic Pollutants Via Peroxydisulfate Activation. *Appl. Catal. B* **2023**, *325*, 122359. [CrossRef]
20. Hu, J.; Zeng, X.; Wang, G.; Qian, B.; Liu, Y.; Hu, X.; He, B.; Zhang, L.; Zhang, X. Modulating Mesoporous Co_3O_4 Hollow Nanospheres with Oxygen Vacancies for Highly Efficient Peroxymonosulfate Activation. *Chem. Eng. J.* **2020**, *400*, 125869. [CrossRef]
21. Cheng, D.; Feng, Y.; Feng, B.; Wang, K.; Song, G.; Wang, G.; Cheng, X.; Deng, Y.; Wei, J. Polyphenol-Mediated Interfacial Deposition Strategy for Supported Manganese Oxide Catalysts with Excellent Pollutant Degradation Performance. *Chin. Chem. Lett.* **2024**, *35*, 109432. [CrossRef]
22. Wen, L.X.; Li, X.P.; Liu, Y.; Liu, M.; Guo, M.X.; Huang, Z.H.; Yang, S.J.; Ding, D.H.; Chen, Y.; Liu, N.; et al. Surface Confinement Boosts the In-Situ Formation of Peroxydisulfate Metastable Complexes on Assembled Hollow N-Rich Carbon Plates for Water Purification. *Appl. Catal. B* **2024**, *358*, 124424. [CrossRef]
23. Huang, B.K.; Wu, Z.L.; Wang, X.H.; Song, X.Y.; Zhou, H.Y.; Zhang, H.; Zhou, P.; Liu, W.; Xiong, Z.K.; Lai, B. Coupled Surface-Confinement Effect and Pore Engineering in a Single-Fe-Atom Catalyst for Ultrafast Fenton-Like Reaction with High-Valent Iron-Oxo Complex Oxidation. *Environ. Sci. Technol.* **2023**, *57*, 15667–15679. [CrossRef] [PubMed]
24. Luo, H.; Zheng, J.L.; Liu, J.X.; Ma, J.J.; He, R.; Huang, C.Q.; Xie, R.; Lin, Q.T. Nanoconfinement-Enhanced Peroxymonosulfate Activation by Co Single Atoms in Hollow Mesoporous Carbon: Roles of Active-Site Chemistry and Mesoscale Confinement. *Water Res.* **2026**, *302*, 126136. [CrossRef] [PubMed]
25. Wang, K.; Wang, R.P.; Zhang, S.Y.; Wang, M.; He, Z.X.; Chen, H.L.; Ho, S.H. Hollow Nanoreactors Unlock New Possibilities for Persulfate-Based Advanced Oxidation Processes. *Small* **2024**, *20*, 2401796. [CrossRef] [PubMed]
26. Lv, R.; Wang, L.Y.; Lan, J.; Zhao, Z.S.; Liu, X.J.; Zhang, C.Y.; Li, G.L. Nanoconfined Co_3O_4 in Hollow Carbon Spheres Unlocks Synergistic Nonradical Pathways for Superior Persulfate Activation. *Chem. Eng. J.* **2025**, *526*, 123456. [CrossRef]
27. Liu, Q.B.; Pang, W.; Chen, X.H.; Diao, P.L.; Tian, W.; Cui, F.; Han, Y.D.; Zhou, H.Y.; Kawi, S. Double-Shelled Hollow Iron-Encapsulated Zeolite for Enhanced Mass Transfer and Reusability in Persulfate Activation. *Chem. Commun.* **2026**, *62*, 11683–11686. [CrossRef] [PubMed]
28. Xie, Y.B.; Liu, Y.; Yao, Y.J.; Shi, Y.C.; Zhao, B.R.; Wang, Y.X. In-Situ Synthesis of N, S Co-Doped Hollow Carbon Microspheres for Efficient Catalytic Oxidation of Organic Contaminants. *Chin. Chem. Lett.* **2022**, *33*, 1298–1302. [CrossRef]
29. Zhang, B.T.; Yan, Z.H.; Zhao, J.J.; Chen, Z.; Liu, Y.C.; Fan, M.H.; Du, W. Peroxymonocarbonate Activation Via Co Nanoparticles Confined in Metal-Organic Frameworks for Efficient Antibiotic Degradation in Different Actual Water Matrices. *Water Res.* **2023**, *243*, 120340. [CrossRef] [PubMed]

30. Chen, C.C.; Zhao, M.Y.; Chen, Y.H.; Jia, W.R.; Wu, Y.H.; Liang, Y.Q.; Du, J.; Wu, Q.L.; Feng, X.C.; Wang, H.Z.; et al. Constructing Nanoconfined Spaces in Persulfate Oxidation Processes for Efficient Degradation of Emerging Contaminants: Structures, Mechanisms, and Challenges. *Sep. Purif. Technol.* **2025**, *354*, 128689. [CrossRef]
31. Sasidharan, M.; Nakashima, K. Core-Shell-Corona Polymeric Micelles as a Versatile Template for Synthesis of Inorganic Hollow Nanospheres. *Acc. Chem. Res.* **2014**, *47*, 157–167. [CrossRef] [PubMed]
32. Zhu, M.Y.; Tang, J.J.; Wei, W.J.; Li, S.J. Recent Progress in the Syntheses and Applications of Multishelled Hollow Nanostructures. *Mater. Chem. Front.* **2020**, *4*, 1105–1149. [CrossRef]
33. Ge, W.J.; Chen, X.C.; Ma, R.Z.; Zheng, S.Y.; Shang, N.Z.; Zhao, X.X. Recent Advances in 0D Ni/Co-Based Hollow Electrocatalysts for Electrochemical Water Splitting. *Chem. Res. Chin. Univ.* **2024**, *40*, 437–450. [CrossRef]
34. Wang, G.; Qin, J.; Zhou, X.; Deng, Y.; Wang, H.; Zhao, Y.; Wei, J. Self-Template Synthesis of Mesoporous Metal Oxide Spheres with Metal-Mediated Inner Architectures and Superior Sensing Performance. *Adv. Funct. Mater.* **2018**, *28*, 1806144. [CrossRef]
35. Wang, G.; Zhou, X.; Qin, J.; Liang, Y.; Feng, B.; Deng, Y.; Zhao, Y.; Wei, J. General Synthesis of Mixed Semiconducting Metal Oxide Hollow Spheres with Tunable Compositions for Low-Temperature Chemiresistive Sensing. *ACS Appl. Mater. Interfaces* **2019**, *11*, 35060–35067. [CrossRef] [PubMed]
36. Wang, G.; Qin, J.; Feng, Y.; Feng, B.; Yang, S.; Wang, Z.; Zhao, Y.; Wei, J. Sol-Gel Synthesis of Spherical Mesoporous High-Entropy Oxides. *ACS Appl. Mater. Interfaces* **2020**, *12*, 45155–45164. [CrossRef] [PubMed]
37. Hussain, M.Z.; Yang, Z.X.; Huang, Z.; Jia, Q.L.; Zhu, Y.Q.; Xia, Y.D. Recent Advances in Metal-Organic Frameworks Derived Nanocomposites for Photocatalytic Applications in Energy and Environment. *Adv. Sci.* **2021**, *8*, 2100625. [CrossRef] [PubMed]
38. Zhou, W.X.; Tang, Y.J.; Zhang, X.Y.; Zhang, S.T.; Xue, H.G.; Pang, H. MOF Derived Metal Oxide Composites and Their Applications in Energy Storage. *Coord. Chem. Rev.* **2023**, *477*, 123456. [CrossRef]
39. Wang, G.; Yang, S.; Cao, L.; Jin, P.; Zeng, X.; Zhang, X.; Wei, J. Engineering Mesoporous Semiconducting Metal Oxides from Metal-Organic Frameworks for Gas Sensing. *Coord. Chem. Rev.* **2021**, *445*, 214086. [CrossRef]
40. Feng, Y.Y.; Yao, Y.; Yue, Q.; Cheng, D.; Wang, O.; Qin, J.; Wei, J. Leavening Inspired Synthesis of Mesoporous High-Entropy Oxide Nanozymes for Detection and Discrimination of Multiple Biological Antioxidants. *Small* **2026**, *22*, e73446. [CrossRef] [PubMed]
41. Feng, B.X.; Feng, Y.Y.; Li, Y.X.; Su, Y.Q.; Deng, Y.H.; Wei, J. Synthesis of Mesoporous Ag_2O/SnO_2 Nanospheres for Selective Sensing of Formaldehyde at a Low Working Temperature. *ACS Sens.* **2022**, *7*, 3963–3972. [CrossRef] [PubMed]
42. Li, P.; Wang, Z.Z.; Feng, Y.Y.; Feng, B.X.; Cheng, D.; Wei, J. Synergistic Sensitization Effects of Single-Atom Gold and Cerium Dopants on Mesoporous SnO_2 Nanospheres for Enhanced Volatile Sulfur Compound Sensing. *Mater. Horiz.* **2024**, *11*, 3038–3047. [CrossRef] [PubMed]
43. Li, S.Y.; Li, J.X.; Wang, X.X.; Sun, Y.F.; Tang, Z.; Gao, X.Y.; Zhang, H.Y.; Xie, J.Z.; Yang, Z.Y.; Yan, Y.M. Energizing Co Active Sites Via d-Band Center Engineering in CeO_2-Co_3O_4 Heterostructures: Interfacial Charge Transfer Enabling Efficient Nitrate Electrosynthesis. *Small* **2024**, *20*, 2311124. [CrossRef] [PubMed]
44. Wang, H.; Wang, D.S.; Sun, C.; Zhao, X.S.; Xu, C.C.; Li, Z.J.; Hou, Y.; Lei, L.C.; Yang, B.; Duan, X.G. Oriented Generation of $^1O_2$ from Peroxymonosulfate Via Co_3O_4 Facet Engineering. *Appl. Catal. B* **2025**, *364*, 124854. [CrossRef]
45. Yan, F.; You, W.H.; Zhou, G.L.; Wei, L.N.; Yang, X.L.; Wu, L.O.; Ke, J.; Wang, L.D. Boosting Peroxymonosulfate Activation for Efficient Acetaminophen Degradation by Oxygen Vacancy-Rich Co_3O_4 Derived from ZIF-67 Via NaBH4 Reduction. *Process Saf. Environ. Prot.* **2026**, *213*, 108978. [CrossRef]
46. Wang, C.; Zou, Y.; Wu, X.; Zhang, X.; Sang, W.; Zhou, T.; Huang, M. Citrate-Ball Milled Cu-Fe Oxides Activate O_2 Triggering Selective Non-Radical Mechanism: A Boosted Strategy Coupling Oxygen Vacancies with Surface Carboxyl. *Chem. Eng. J.* **2025**, *518*, 164580. [CrossRef]
47. *GB 3838-2002*; Chinese National Standard for Surface Water Quality. Ministry of Ecology and Environment: Beijing, China, 2002.
48. Peng, Y.H.; Zhang, Q.M.; Ren, W.; Duan, X.G.; Ding, L.; Jing, Y.P.; Shao, P.H.; Xiao, X.; Luo, X.B. Thermodynamic and Kinetic Behaviors of Persulfate-Based Electron-Transfer Regime in Carbocatalysis. *Environ. Sci. Technol.* **2023**, *57*, 19012–19022. [CrossRef] [PubMed]
49. Wu, S.H.; Zhao, Y.J.; Sun, R.R.; Sun, Z.Q.; Yang, C.P.; Ma, J. Chemistry, Generation and Regulation of Reactive Species in Persulfate-Based Advanced Oxidation Processes. *Chem. Eng. J.* **2025**, *515*, 163588. [CrossRef]
50. Li, N.; Hao, Y.K.; Liang, L.; Wan, S.Q.; Zhao, J.H.; Yan, B.B.; Chen, G.Y. A Critical Review on Persulfate-Based Catalytic Systems: Deactivation Mechanisms and Regulation Strategies. *Water Res.* **2026**, *302*, 126193. [CrossRef] [PubMed]
51. Zhang, P.P.; Yang, Y.Y.; Duan, X.G.; Liu, Y.J.; Wang, S.B. Density Functional Theory Calculations for Insight Into the Heterocatalyst Reactivity and Mechanism in Persulfate-Based Advanced Oxidation Reactions. *ACS Catal.* **2021**, *11*, 11129–11159. [CrossRef]
52. Li, Y.A.; Wei, J.; Cui, N.; Li, J.M.; Xu, M.D.; Pan, G.P.; Jiang, Z.J.; Cui, X.R.; Niu, X.R.; Li, J. Recent Advance of Atomically Dispersed Dual-Metal Sites Carbocatalysts: Properties, Synthetic Materials, Catalytic Mechanisms, and Applications in Persulfate-Based Advanced Oxidation Process. *Adv. Funct. Mater.* **2023**, *33*, 2305678. [CrossRef]

53. Yan, Y.Q.; Wei, Z.S.; Duan, X.G.; Long, M.C.; Spinney, R.; Dionysiou, D.D.; Xiao, R.Y.; Alvarez, P.J.J. Merits and Limitations of Radical Vs. Nonradical Pathways in Persulfate-Based Advanced Oxidation Processes. *Environ. Sci. Technol.* **2023**, *57*, 12153–12179. [CrossRef] [PubMed]
54. Nie, C.Y.; Dai, Z.H.; Meng, H.; Duan, X.G.; Qin, Y.L.; Zhou, Y.B.; Ao, Z.M.; Wang, S.B.; An, T.C. Peroxydisulfate Activation by Positively Polarized Carbocatalyst for Enhanced Removal of Aqueous Organic Pollutants. *Water Res.* **2019**, *166*, 115043. [CrossRef] [PubMed]
55. Govindan, K.; Kim, D.G.; Ko, S.O. Role of Co-Existing Anions in Non-Radical and Radical Processes of Carbocatalyzed Persulfate Activation for Acetaminophen Degradation. *Environ. Sci. Water Res. Technol.* **2022**, *8*, 2940–2955. [CrossRef]
56. Huang, M.; Liu, H.Z.; Huang, Q.Q.; Zhou, T.; Wu, X.; Li, W.W.; Yu, H.Q. Self-Activated Heterogeneous Fenton Process for Accelerated Degradation of Aromatic Pollutants Over Copper Oxide Catalysts. *Angew. Chem. Int. Ed.* **2025**, *64*, e202508754. [CrossRef] [PubMed]
57. Zhang, T.; Zhu, H.; Croué, J.P. Production of Sulfate Radical from Peroxymonosulfate Induced by a Magnetically Separable $CuFe_2O_4$ Spinel in Water: Efficiency, Stability, and Mechanism. *Environ. Sci. Technol.* **2013**, *47*, 2784–2791. [CrossRef] [PubMed]
58. Wang, G.; Ge, L.; Liu, Z.; Zhu, X.; Yang, S.; Wu, K.; Jin, P.; Zeng, X.; Zhang, X. Activation of Peroxydisulfate by Defect-Rich CuO Nanoparticles Supported on Layered MgO for Organic Pollutants Degradation: An Electron Transfer Mechanism. *Chem. Eng. J.* **2022**, *431*, 134026. [CrossRef]
59. Liu, Z.; Wang, K.; Li, D.; Wang, Z.; Yang, S.; Pang, H.; Wang, G.; Ding, D.; Miao, D. Nonradical Activation of Peroxydisulfate Over Fe/N Doped Mesoporous Carbon for Selective Removal of Organic Pollutant. *J. Environ. Chem. Eng.* **2023**, *11*, 109460. [CrossRef]
60. Ren, W.; Xiong, L.; Yuan, X.; Yu, Z.; Zhang, H.; Duan, X.; Wang, S. Activation of peroxydisulfate on carbon nanotubes: Electron-transfer mechanism. *Environ. Sci. Technol.* **2019**, *53*, 14595–14603. [CrossRef] [PubMed]
61. Yan, H.C.; Lai, C.; Liu, S.Y.; Wang, D.B.; Zhou, X.R.; Zhang, M.M.; Li, L.; Li, X.P.; Xu, F.H.; Nie, J.X. Metal-Carbon Hybrid Materials Induced Persulfate Activation: Application, Mechanism, and Tunable Reaction Pathways. *Water Res.* **2023**, *234*, 119808. [CrossRef] [PubMed]
62. Ren, W.; Xiong, L.; Nie, G.; Zhang, H.; Duan, X.; Wang, S. Insights into the electron-transfer regime of peroxydisulfate activation on carbon nanotubes: The role of oxygen functional groups. *Environ. Sci. Technol.* **2020**, *54*, 1267–1275. [CrossRef] [PubMed]
63. Liu, Y.; Zhou, A.J.; Duan, C.M.; Tian, J.; Wang, J.L. Dynamic Structural Evolution of Carbon Catalysts During Persulfate Activation Rewires Nonradical Pathways for Water Decontamination. *Water Res.* **2026**, *301*, 123456. [CrossRef] [PubMed]
64. Jawad, A.; Zhan, K.; Wang, H.B.; Shahzad, A.; Zeng, Z.H.; Wang, J.; Zhou, X.Q.; Ullah, H.; Chen, Z.L.; Chen, Z.Q. Tuning of Persulfate Activation from a Free Radical to a Nonradical Pathway Through the Incorporation of Non-Redox Magnesium Oxide. *Environ. Sci. Technol.* **2020**, *54*, 2476–2488. [CrossRef] [PubMed]
65. Wu, Y.N.; Huang, D.H.; Li, D.X.; Qian, X.B.; Niu, J.F. From Ambiguity to Application: Deciphering Non-Radical Pathways in Heterogeneous Persulfate Activation. *Adv. Mater.* **2026**, *38*, 2405678. [CrossRef] [PubMed]
66. Zhu, H.; Ma, H.; Yu, J.; Zhao, Z.; Xu, L.; Li, X.; Rao, Y.; Lai, B.; Pu, S. Encapsulating MnFe LDH in Biochar Tunes Persulfate Activation from Radical to Nonradical Pathway: Significant Role of Electron Transfer. *ACS EST Water* **2023**, *3*, 3343–3356. [CrossRef]
67. Yang, Y.; Ren, W.; Hu, K.; Zhang, P.; Wang, Y.; Duan, X.; Sun, H.; Wang, S. Challenges in Radical/Nonradical-Based Advanced Oxidation Processes for Carbon Recycling. *Chem. Catal.* **2022**, *2*, 1858–1869. [CrossRef]
68. Bai, L.; Zhang, J.; He, J.; Zheng, H.; Yang, Q. ZnO-Co_3O_4/N-C cage derived from hollow Zn/Co ZIF for enhanced degradation of BPA with persulfate. *Inorg. Chem.* **2021**, *60*, 13041–13050. [CrossRef] [PubMed]
69. Ma, Q.; Zhang, Y.; Zhu, X.; Chen, B. Hollow multi-shelled Co_3O_4 as nanoreactors to activate peroxymonosulfate for highly effective degradation of carbamazepine: A novel strategy to reduce nano-catalyst agglomeration. *J. Hazard. Mater.* **2022**, *427*, 127890. [CrossRef] [PubMed]
70. Liu, D.; Li, M.; Li, X.; Ren, F.; Sun, P.; Zhou, L. Core-shell Zn/Co MOFs derived Co_3O_4/CNTs as an efficient magnetic heterogeneous catalyst for persulfate activation and oxytetracycline degradation. *Chem. Eng. J.* **2020**, *404*, 124008. [CrossRef]
71. Wang, M.; Cui, Y.; Cao, H.; Wei, P.; Chen, C.; Li, X.; Xu, J.; Sheng, G. Activating peroxydisulfate with Co_3O_4/$NiCo_2O_4$ double-shelled nanocages to selectively degrade bisphenol A-A nonradical oxidation process. *Appl. Catal. B Environ.* **2021**, *282*, 119585. [CrossRef]
72. Khan, M.A.N.; Klu, P.K.; Wang, C.; Zhang, W.; Luo, R.; Zhang, M.; Qi, J.; Sun, X.; Wang, L.; Li, J. Metal-organic framework-derived hollow Co_3O_4/carbon as efficient catalyst for peroxymonosulfate activation. *Chem. Eng. J.* **2019**, *363*, 234–246. [CrossRef]

Disclaimer/Publisher's Note: The statements, opinions and data contained in all publications are solely those of the individual author(s) and contributor(s) and not of MDPI and/or the editor(s). MDPI and/or the editor(s) disclaim responsibility for any injury to people or property resulting from any ideas, methods, instructions or products referred to in the content.